

Article

Metallosupramolecular Polymer Precursor Design for Multi-Element Co-Doped Carbon Shells with Improved Oxygen Reduction Reaction Catalytic Activity

Yuzhe Wu, Yuntong Li, Jie Mao, Haiyang Wu, Tong Wu, Yaying Li, Birong Zeng, Yiting Xu, Conghui Yuan *  and Lizong Dai *

Fujian Provincial Key Laboratory of Fire Retardant Materials, College of Materials, Xiamen University, Xiamen 361005, China; wuyuzhe@stu.xmu.edu.cn (Y.W.); lyt@stu.xmu.edu.cn (Y.L.); mao-jie@foxmail.com (J.M.); why@stu.xmu.edu.cn (H.W.); wutong@stu.xmu.edu.cn (T.W.); liyaying@stu.xmu.edu.cn (Y.L.); brzeng@xmu.edu.cn (B.Z.); xyting@xmu.edu.cn (Y.X.)

* Correspondence: yuanch@xmu.edu.cn (C.Y.); lzdai@xmu.edu.cn (L.D.); Tel.: +86-592-2186178 (C.Y. & L.D.)

Received: 10 December 2018; Accepted: 15 January 2019; Published: 18 January 2019



Abstract: Heteroatom-doped carbon materials have been extensively studied in the field of electrochemical catalysis to solve the challenges of energy shortage. In particular, there is vigorous research activity in the design of multi-element co-doped carbon materials for the improvement of electrochemical performance. Herein, we developed a supramolecular approach to construct metallosupramolecular polymer hollow spheres, which could be used as precursors for the generation of carbon shells co-doped with B, N, F and Fe elements. The metallosupramolecular polymer hollow spheres were fabricated through a simple route based on the Kirkendall effect. The in situ reaction between the boronate polymer spheres and Fe^{3+} could easily control the component and shell thickness of the precursors. The as-prepared multi-element co-doped carbon shells showed excellent catalytic activity in an oxygen reduction reaction, with onset potential (E_{onset}) 0.91 V and half-wave ($E_{\text{half-wave}}$) 0.82 V vs reversible hydrogen electrode (RHE). The fluorine element in the carbon matrix was important for the improvement of oxygen reduction reaction (ORR) activity performance through designing the control experiment. This supramolecular approach may afford a new route to explore good activity and a low-cost catalyst for ORR.

Keywords: carbon shell; metallosupramolecular polymer; hollow particles; doping; oxygen reduction reaction

1. Introduction

During the commercialization process of hydrogen fuel cells, exploring electrocatalysts with high oxygen reduction reaction (ORR) activity and outstanding stability is the primary task [1–3]. At present, precious metals incorporating carbon materials, such as commercial Pt/C, have been successfully used as ORR catalysts [4,5]. However, their expensive cost and scarcity greatly limit their broader application [6–8]. Therefore, fabricating non-precious metal composite materials with low-cost, and a catalytic performance comparable or better than commercial Pt/C toward ORR, is of great significance to commercial applications [9,10].

Pure carbon materials have many advantages, including excellent electrical transport properties, a highly active surface area, chemical stability and superior thermal stability. They have thus become an ideal choice for electrochemical energy storage materials [11–15]. However, pure carbon materials have a highly hydrophobic surface and limited active sites, which bring many problems for the application

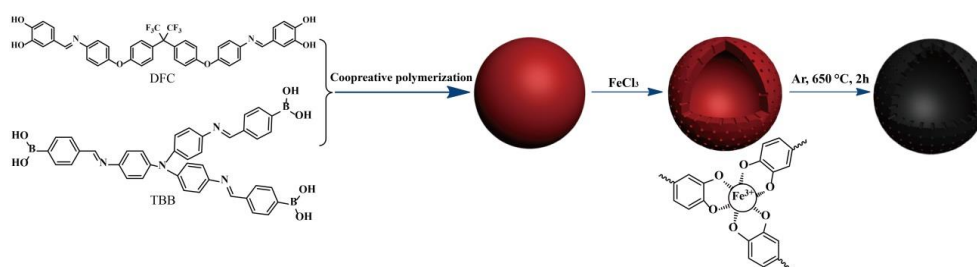
in hydrogen fuel cells. Heteroatom-doping has been recognized as an effective approach to increase the electrochemical activity and surface wettability of carbon materials [16,17]. The chemical elements used for doping carbon materials include nitrogen, phosphorus, boron, fluorine and non-precious metals [18–22]. Notably, N, B co-doped carbon materials have shown excellent ORR performance, because they possess large amounts of defects and active sites [23,24]. Except for the heteroatom-doping materials, carbon materials incorporated with metal and N elements (M–N–C) have been considered as one of the promising candidates. Most of the M–N–C catalysts were prepared via heat-treating the carbon materials with an N-containing compound, as well as metal salts, or obtained from the simple pyrolysis of transition metal macrocyclic polymers [25–27]. Nevertheless, these approaches have shortcomings, such as inhomogeneity of the carbon materials, the aggregation of the active sites, complicated synthesis, as well as high-cost [28,29]. Hence, there exists a need to develop a facile and effective route to fabricate polymeric precursors, containing multiple elements like B, P, S, F, Co and Fe. This is of great importance to incorporate multi-elements into the carbon materials.

We have developed a supramolecular approach, in which the condensation reaction between boronic and catechol monomers is accompanied with the formation of B–N dative bonds, and can organize as formed boronate polymers into nanospheres with controllable sizes [30]. The catechol moiety has a high coordination efficiency with transition metal ions and the Kirkendall effect occurs during the reaction between boronate polymer nanospheres and transition metal ions, thus resulting in the formation of metallosupramolecular polymer hollow spheres [31]. In this work, we extended this approach through the design of the building blocks of the boronate polymers, and therefore metallosupramolecular polymer hollow sphere precursors, containing B, N, F and Fe elements, could be fabricated. Carbonation of the metallosupramolecular polymer hollow sphere precursor at 650 °C afforded carbon shells co-doped with B, N, F and Fe elements. We focused on the control over the thickness of the shell, the influence of the shell thickness and doping elements (B, N, F and Fe) on the ORR performance of the carbon materials.

2. Results and Discussion

2.1. Morphology Evolution

The synthetic process of carbon spheres (CSs) is shown in Scheme 1. We firstly prepared the boronate polymer nanospheres through a simple condensation reaction between 4,4'-((1E,1'E)-(((perfluoropropane-2,2-diyl)bis(4,1-phenylene))bis(oxy))bis(4,1-phenylene))bis(azanylylidene))bis(methanylylidene))bis(benzene-1,2-diol) (DFC) and (((1E,1'E,1''E)-((nitrilotris(benzene-4,1-diyl))tris(azanylylidene))tris(methanylylidene)) tris(benzene-4,1-diyl))triboronic acid (TBB). The catechol moiety has a high coordination ability to transition metal ions. This coordination interaction is of particular interest in the fabrication of supramolecular polymers, assemblies, smart hydrogels and metal–organic frameworks [32–34]. Since the boronate moiety is dynamic, there probably existed free catechol groups in our boronate polymer nanospheres. Thus, we intended to introduce Fe³⁺ into the boronate polymer nanoparticles through the catechol–Fe³⁺ coordination, thereby forming metallosupramolecular polymers, which comprise Fe, N, B and F elements. After carbonization, carbon materials co-doped with Fe, N, B and F could be obtained.



Scheme 1. Synthetic process of the carbon spheres (CSs).

With the assistance of the B–N coordination, a cross-linking reaction between DFC and TBB adopted a typical cooperative polymerization mechanism, and therefore, mono-dispersed boronate polymer nanospheres (BPN) could be formed in one-step (Figure 1a,b) [30]. The coordination reaction between catechol and Fe^{3+} could evidently change the morphology of the boronate polymer nanospheres, which accorded well with a previous report [31]. The metallosupramolecular polymer could be easily carbonized to afford CSs with hollow structures.

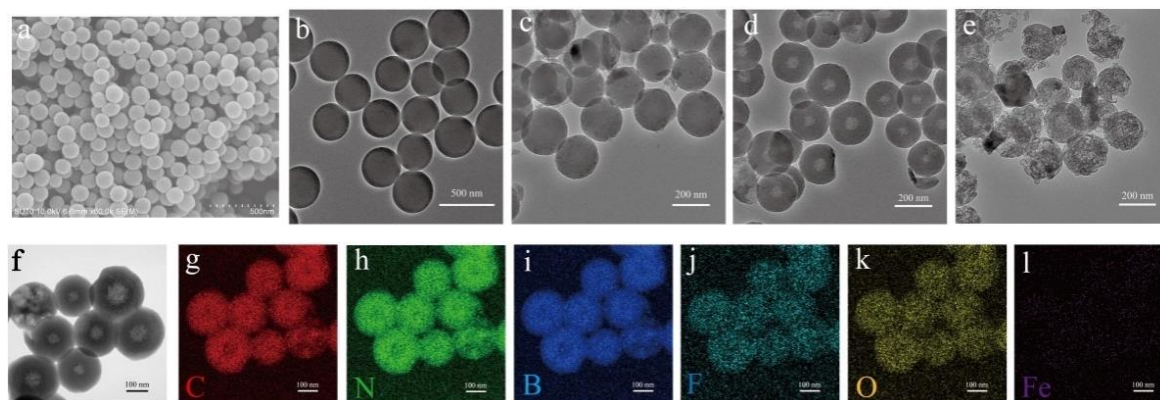


Figure 1. SEM (a) and TEM (b) images of boronate polymer nanosphere (BPN) nanoparticles. TEM images of CS₆₋₆₅₀ (c), CS₁₂₋₆₅₀ (d) and CS₁₈₋₆₅₀ (e). High-angle annular dark-field imaging scanning transmission electron microscope (HAADF-STEM) image (f) and corresponding energy-dispersive X-ray (EDX) mappings (g–l) of CS₁₂₋₆₅₀.

Figure 1c–e show the TEM images of the CSs prepared from precursors derived from different reaction times. Small pores were created in the interior of the nanospheres within a 6 h reaction time (Figure 1c). When the reaction time was 12 h, hollow nanospheres with shell thickness ~ 70 nm were obtained (Figure 1d). However, too long of a reaction time was likely to destroy the nanospheres, because many of the obtained particles collapsed (Figure 1e). As demonstrated by the previous report, hollow structural metallosupramolecular polymer precursors were generated according to the Kirkendall effect during the reaction between boronate polymer nanospheres and Fe^{3+} [31]. This process greatly relied on the removal of the boronic acid component. Too long of a reaction time between the boronate polymer nanospheres and Fe^{3+} can result in excessive removal of the boronic acid component, therefore leading to the collapse of the particles. Dark-field TEM imaging of carbon particles obtained from a 12 h reaction time between the boronate polymer nanospheres and Fe^{3+} confirmed the hollow structure (Figure 1f). Energy-dispersive X-ray (EDX) mapping of representative hollow particles indicated the coexistence of C, N, B, F, O and Fe elements (Figure 1g–l). The carbonization temperature likely had no evident effect on the morphology of the carbon materials, as the TEM images of CS₁₂₋₅₅₀ and CS₁₂₋₇₅₀ (Figure S1), display similar morphology to CS₁₂₋₆₅₀.

2.2. Composition and Structure Characterization

Figure 2a gives the Raman spectra of the CSs. The two prominent peaks at 1340 and 1571 cm^{-1} represent the D band of disordered graphitic structure and the G band of ordered carbon matrix, respectively. The calculated intensity ratio from the D band and the G band (I_D/I_G) was applied to evaluate the disorder degree of the carbon materials. The calculated I_D/I_G value of CS₆₋₆₅₀, CS₁₂₋₆₅₀ and CS₁₈₋₆₅₀ were 1.22, 1.26 and 1.29, respectively. Probably, the content defect site in the carbon materials increased with the increasing reaction between BPN and Fe^{3+} . The calculated I_D/I_G value of CS₁₂₋₅₅₀ and CS₁₂₋₇₅₀ were 0.94 and 1.19, respectively, which were lower than that of CS₁₂₋₆₅₀.

The crystalline structures of CSs were characterized through XRD. As shown in Figure 2b, an evident broad diffraction peak located at about 25° could be attributed to the (002) plane of ordered graphitic structure. The sharp peak at about 45° was the (110) plane of iron, reduced by the

hydrogen–argon mixture gas. Two broad diffraction peaks at about 35° and 43° were derived from the (311) and (222) planes of Fe_3O_4 [35]. With the elongation of reaction time between BPN and Fe^{3+} , the characteristic peaks of both iron and Fe_3O_4 were obviously enhanced. It is likely that penetration of Fe^{3+} into BPN and formation of metallosupramolecular polymers was time dependent. The effect of carbonization temperature on the crystalline structure of CSs was studied by XRD. CSs obtained from different carbonization temperatures generally had similar peak positions. However, with the carbonization temperature increased from 550°C to 750°C , the shape, width and intensity of the peak at 25° changed. Therefore, the carbonization temperature could affect the carbon matrix crystalline structure of CSs. It was observed that CS_{12-650} prepared by the carbonization temperature of 650°C had the best crystallinity.

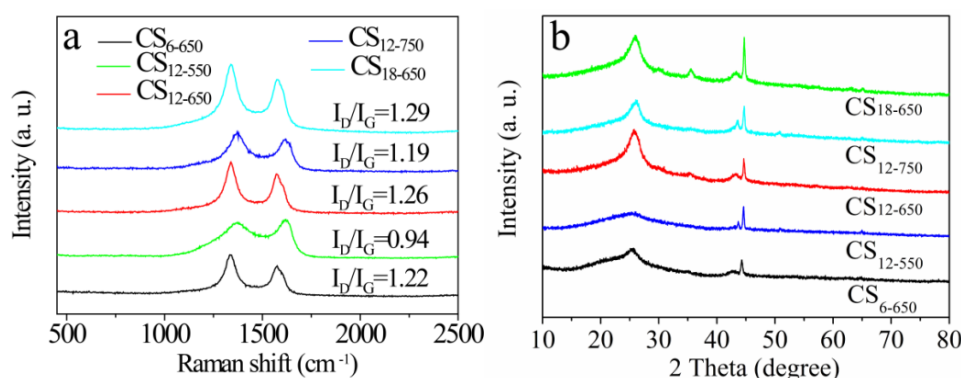


Figure 2. Raman spectra (a) and XRD patterns (b) of CSs.

The pore character of CSs was tested by physisorption of nitrogen at 77 K. As shown in Figure 3, CSs comprise both microporous and mesoporous structures. Detailed Brunauer–Emmett–Teller (BET) data is also listed in Table 1. The surface areas of CS_{6-650} , CS_{12-650} and CS_{18-650} are 361.62 , 439.47 and $451.13\text{ m}^2\text{ g}^{-1}$, with relative pore volumes of 0.34 , 0.40 and $0.36\text{ cm}^3\text{ g}^{-1}$, respectively. Obviously, their surface areas mainly resulted from the microporous- and mesoporous-pore structures. The specific surface area of the CSs increased gradually with the increase of reaction for the generation of the precursor. The mesoporous-pore volumes of CS_{6-650} , CS_{12-650} and CS_{18-650} were 212.08 , 258.68 and $190.00\text{ m}^2\text{ g}^{-1}$, respectively. Apparently, CS_{12-650} had the maximum mesoporous-pore compared with CS_{6-650} and CS_{18-650} . The mesoporous-pore is important and beneficial for ORR. The surface areas of CS_{12-550} and CS_{12-750} were 394.38 and $445.20\text{ m}^2\text{ g}^{-1}$, with relative pore volumes of 0.34 and $0.35\text{ cm}^3\text{ g}^{-1}$ (Table 1), respectively, which were lower than that of CS_{12-650} and CS_{18-650} . This result indicated that the precursor might be not completely carbonized at 550°C , and a carbonization temperature of 750°C was not helpful for the development of the pore structure.

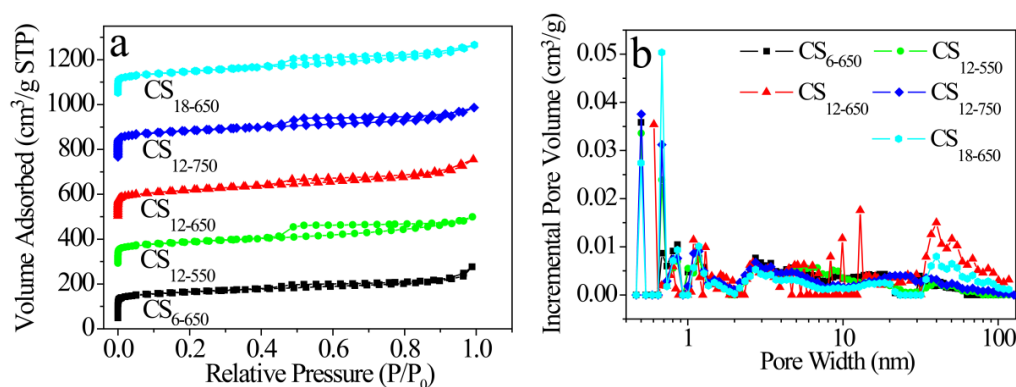


Figure 3. N_2 adsorption and desorption isotherms (a) and density functional theory (DFT) pore size distribution (b) of CSs.

Table 1. Surface area, porosity of CSs.

Samples	S_{BET}^a [$\text{m}^2 \text{g}^{-1}$]	S_{micro}^b [$\text{m}^2 \text{g}^{-1}$]	$S_{\text{meso} + \text{macro}}^c$ [$\text{m}^2 \text{g}^{-1}$]	V_{total}^d [$\text{cm}^3 \text{g}^{-1}$]
CS ₆₋₆₅₀	361.62	149.54	212.08	0.34
CS ₁₂₋₅₅₀	394.38	182.54	211.84	0.34
CS ₁₂₋₆₅₀	439.47	180.79	258.68	0.40
CS ₁₂₋₇₅₀	445.20	178.97	266.23	0.35
CS ₁₈₋₆₅₀	451.13	261.13	190.00	0.36

^a Specific surface area obtained from BET, ^b Surface area of micropores calculated by the t-plot method, ^c Surface area of mesopores and macropores calculated by the t-plot method, ^d Total pore volume.

The X-ray photoelectron spectroscopy (XPS) survey spectra of CS₆₋₆₅₀, CS₁₂₋₆₅₀ and CS₁₈₋₆₅₀ are shown in Figure 4a. In addition, the high-resolution XPS spectra of C 1s, N 1s, B 1s, F 1s and Fe 2p of CS₁₂₋₆₅₀ were characterized (Figure 4b–f). The C 1s signal can be split into four representative peaks at about 288.2 (C=O), 285.4 (C–O, C–N), 284.4 (C–C, C=C) and 283.6 eV (C–B) (Figure 4b). The six peaks of N 1s spectrum shown in Figure 4c at 403.2, 401.3, 400.3, 399.4, 398.3 and 397.7 eV are attributed to oxidized N, graphitic N, pyrrolic N, amine, pyridinic N, as well as N–B [23]. Notably, pyridinic N was recognized to produce excellent oxygen reduction reaction activity [24]. Three typical peaks of B 1s at 192.1, 190.8 and 189.2 eV were assigned to B–O, B–N, B–C (Figure 4d), separately [36]. The F 1s signal is displayed in Figure 4e. This indicated that fluorine remains in the carbon matrix. The weak peak at 685.7 eV was assigned to the F[−] anions. The existence of the F element had the ability to accelerate the oxygen reduction reaction process of carbon catalysts [37]. For the Fe 2p spectrum shown in Figure 4f, the peak at 723.2 eV was assigned to the binding energy of Fe²⁺, and the peak for Fe³⁺ was detected at 725.4 eV for the 2p_{1/2} band. Another two peaks at 714.4 and 710.5 eV could be respectively attributed to the binding energies of the 2p_{3/2} orbitals of Fe³⁺ and Fe²⁺ species [38]. The Fe 2p_{3/2} peak at approximately 703.5 eV corresponded to Fe⁰. The last peak at 719.6 eV was a satellite peak. The XPS results, in combination with the XRD results, clearly confirmed that only a small amount of iron element was transformed into Fe₃O₄, and most of iron element was changed into zero-valent iron, which may be of potential in improving the electrical conductivity of the carbon materials.

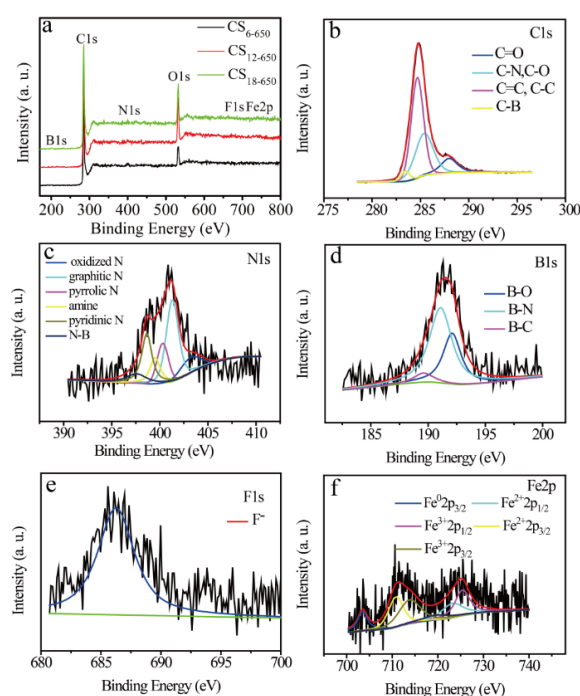


Figure 4. X-ray photoelectron spectroscopy (XPS) survey spectra of CS₆₋₆₅₀, CS₁₂₋₆₅₀ and CS₁₈₋₆₅₀ (a). High-resolution XPS spectra of (b) C 1s, (c) N 1s, (d) B 1s and (e) F 1s, (f) Fe 2p for the CS₁₂₋₆₅₀.

The XPS survey spectra of CS₁₂₋₅₅₀ and CS₁₂₋₇₅₀ are shown in Figure S2. CS₁₂₋₅₅₀ obtained at 550 °C had F content of 0.94%. However, at carbonization temperature of 750 °C, the prepared CS₁₂₋₇₅₀ comprised no fluorine element (Table S1). Because the C–F bond in the precursor accorded to a regular fracture, the temperature of 650 °C was the highest temperature that could retain the fluorine element in the carbon matrix, as well as endow the materials with adequate carbonization.

2.3. ORR Performances

We then tested the electrochemical performance of the CSs to evaluate their potential as ORR electrocatalysts. The cyclic voltammetry (CV) curves of CS₆₋₆₅₀, CS₁₂₋₆₅₀ and CS₁₈₋₆₅₀ were tested in Ar- or O₂-saturated 0.1 M KOH solution (Figure 5a). All samples only displayed an obvious reduction peak in O₂-saturated solution. The linear sweep voltammetry (LSV) curves of CSs are shown in Figure 5b–d. The onset potential (E_{onset}) of CS₆₋₆₅₀, CS₁₂₋₆₅₀ and CS₁₈₋₆₅₀ for the oxygen reduction reaction were 0.83 V, 0.91 V and 0.78 V, respectively. The half-wave ($E_{\text{half-wave}}$) potentials of CS₆₋₆₅₀, CS₁₂₋₆₅₀ and CS₁₈₋₆₅₀ for the oxygen reduction reaction were 0.79 V, 0.82 V and 0.76 V. This result was also confirmed by a LSV test in the O₂-saturated 0.1 M KOH solution, at a rotation rate of 1600 rpm, with a scan rate of 10 mV/s (Figure 5e). On the other hand, the catalytic activity of the commercial 20 wt% Pt/C was tested under identical experimental conditions (Figure 5e). In comparison, the E_{onset} and $E_{\text{half-wave}}$ of CS₁₂₋₆₅₀ were 0.91 V and 0.82 V, respectively, which were close to that of the commercial 20 wt% Pt/C catalyst with the onset and half-wave potentials of 0.95 V and 0.85 V vs. RHE.

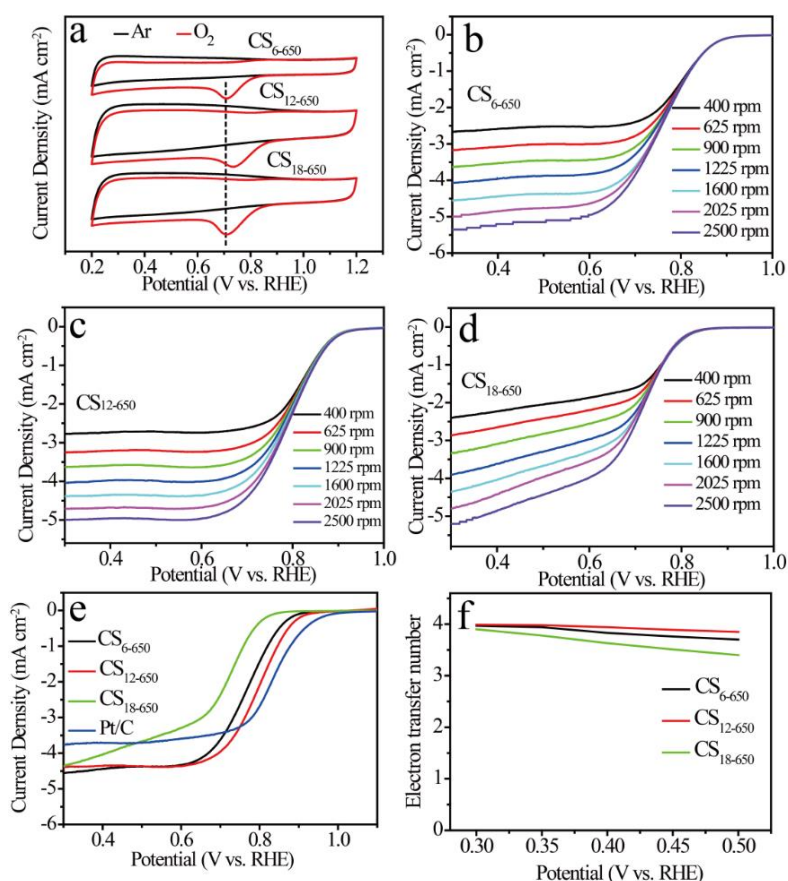


Figure 5. CV curves of CS₆₋₆₅₀, CS₁₂₋₆₅₀ and CS₁₈₋₆₅₀ in Ar- or O₂-saturated 0.1 M KOH aqueous solution at a scan rate of 50 mV/s (a). Linear sweep voltammetry (LSV) curves of CS₆₋₆₅₀ (b), CS₁₂₋₆₅₀ (c) and CS₁₈₋₆₅₀ (d) in O₂-saturated 0.1 M KOH aqueous solution at different rotation speeds. LSV curves of CS₆₋₆₅₀, CS₁₂₋₆₅₀ and CS₁₈₋₆₅₀ and the commercial 20 wt% Pt/C in O₂-saturated 0.1 M KOH aqueous solution at a rotation rate of 1600 rpm and a scan rate of 10 mV/s (e). Electron transfer numbers obtained from The Koutecky–Levich (K–L) plots of CS₆₋₆₅₀, CS₁₂₋₆₅₀ and CS₁₈₋₆₅₀ (f).

The evidently improved electrocatalytic performance of CS₁₂₋₆₅₀ could be explained by the following two reasons. First, CS₁₂₋₆₅₀ had relatively higher specific surface area compared with CS₆₋₆₅₀ as proved by BET results, thus leading to the exposure of more active sites. CS₁₂₋₆₅₀ also had a higher content of mesoporous-pore than CS₆₋₆₅₀ and CS₁₈₋₆₅₀, and the mesoporous-pore was beneficial for ORR. Second, CS₁₂₋₆₅₀ had relatively thin shell thickness and a regular hollow morphology, which was beneficial for the transfer of water and oxygen during the catalytic reaction. As illustrated by the LSV results, the second platform of the LSV curves of CS₁₂₋₆₅₀ became very flat in comparison with CS₁₈₋₆₅₀, indicating the equilibrium of the catalytic reaction. As the morphology of CS₁₈₋₆₅₀ was completely damaged and collapsed, the irregular structure could have increased the specific surface area of CS₁₈₋₆₅₀ to some extent, but also could have prevented the generation and loading of active sites during carbonization. The activity of CS₁₈₋₆₅₀ was thus reduced. Therefore, we consider that a synergistic effect between surface area, shell thickness, morphology and enough available active sites, directly led to the optimization of ORR catalytic activity of CS₁₂₋₆₅₀.

The LSV curves at different rotating rates were tested to study the reaction kinetics of the ORR catalyzed by CSs. The current density of CS₆₋₆₅₀, CS₁₂₋₆₅₀ and CS₁₈₋₆₅₀ increased when increasing the rotating rate from 400 to 2500 rpm, as shown in Figure 5b–d. This could be attributed to the decrease of the diffusion distance. The Kouteckye–Levich (K–L) plots were calculated from the above LSV curves, which revealed a clear linear relationship and quite similar slopes at the corresponding potential, ranging from 0.3 V to 0.5 V (Figure S3a–c). Obviously, the ORR catalyzed by CSs accorded classic first-order reaction kinetics. By calculating underlying slope shown in Figure 5f, the electron transfer numbers (*n*) derived from the corresponding slopes of Kouteckye–Levich (K–L) plots were approximately 3.94 for CS₆₋₆₅₀, 3.96 for CS₁₂₋₆₅₀ and 3.88 for CS₁₈₋₆₅₀, verifying an atypical four-electron transfer process. This is the same as the many reported B and N elements co-doped carbon materials [23,24,39].

The CV curves of CS₁₂₋₅₅₀ and CS₁₂₋₇₅₀ were also tested in Ar- or O₂-saturated 0.1 M KOH solution (Figure 6a), and the corresponding LSV curves of CS₁₂₋₅₅₀ and CS₁₂₋₇₅₀ are shown in Figure 6b,c. The onset potential (*E*_{onset}) of CS₁₂₋₅₅₀ and CS₁₂₋₇₅₀ were 0.85 V and 0.86 V. The half-wave (*E*_{half-wave}) potentials of CS₁₂₋₅₅₀ and CS₁₂₋₇₅₀ were 0.74 V and 0.77 V. In comparison, the *E*_{onset} and *E*_{half-wave} of CS₁₂₋₆₅₀ were 0.91 V and 0.82 V, respectively, which were much better than the CS₁₂₋₅₅₀ and CS₁₂₋₇₅₀. The electron transfer numbers (*n*) derived from the corresponding slopes of Kouteckye–Levich (K–L) plots (Figure S3d–f) were approximately 3.26 for CS₁₂₋₅₅₀ and 3.56 for CS₁₂₋₇₅₀, verifying a typical four-electron transfer process.

Since they were derived from the same precursor, we considered that the carbonization temperature could evidently affect the ORR performance of the CSs. First, CS₁₂₋₆₅₀ had higher *I*_D/*I*_G value than CS₁₂₋₅₅₀ and CS₁₂₋₇₅₀, implying more defect sites in the carbon matrix. Second, CS₁₂₋₆₅₀ had relatively higher specific surface area relative to CS₁₂₋₅₅₀, as proved by BET results, and thus lead to the exposure of more active sites. The specific surface area of CS₁₂₋₆₅₀ and CS₁₂₋₇₅₀ was nearly the same, so CS₁₂₋₆₅₀ and CS₁₂₋₇₅₀ had the same utilization towards the active site in the same condition. Third, comparing CS₁₂₋₆₅₀ and CS₁₂₋₇₅₀, the existence of the fluorine element in CS₁₂₋₆₅₀ was important for the improved ORR performance of CS₁₂₋₆₅₀. Therefore, we considered that the fluorine element in the carbon matrix could promote the generation of defect sites, which was beneficial and important for the ORR activity.

The durability of CS₁₂₋₆₅₀ was tested at 1600 rpm in O₂-saturated 0.1 M KOH aqueous solution after 1000 cycles of CV curves (Figure 7a). The onset and half-wave potentials of CS₁₂₋₆₅₀ were kept at 0.90 V and 0.80 V. No evident current decrease in the onset and half-wave potentials was observed. The attenuation of electrocatalytic activity was less than 5%, which was much better than the commercial 20 wt% Pt/C catalysts (as shown in Figure S4). Thus, CSs had preferable durability for ORR in the alkaline condition. The relevant crossover effects test was also carried out by taking CS₁₂₋₆₅₀ as an example through a chronoamperometric experiment. After adding 3.0 M methanol, the methanol oxidation reaction made the current density of the commercial Pt/C decrease immediately (Figure 7b).

However, the current density of CS₁₂₋₆₅₀ did not display an evident change. These results directly confirmed that CS₁₂₋₆₅₀ has good catalytic selectivity for the oxygen reduction reaction.

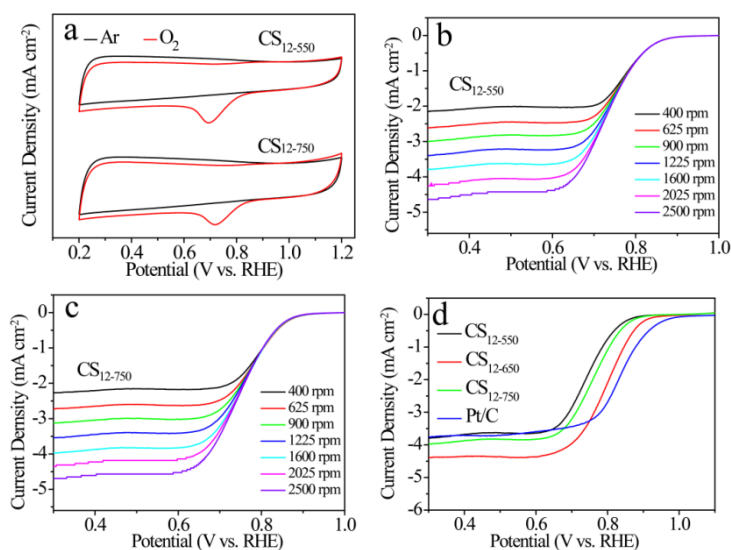


Figure 6. CV curves of CS₁₂₋₅₅₀ and CS₁₂₋₇₅₀ in Ar- or O₂-saturated 0.1 M KOH aqueous solution with a scan rate of 50 mV/s (a). LSV curves of CS₁₂₋₅₅₀ (b) and CS₁₂₋₇₅₀ (c) and (d) LSV curves of CS₁₂₋₅₅₀, CS₁₂₋₆₅₀ and CS₁₂₋₇₅₀ and the commercial 20 wt% Pt/C in O₂-saturated 0.1 M KOH aqueous solution at a rotation rate of 1600 rpm and a scan rate of 10 mV/s.

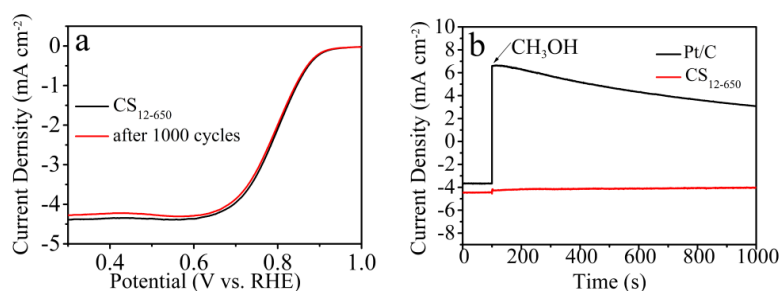


Figure 7. LSV curves of the CS₁₂₋₆₅₀ at 1600 rpm in O₂-saturated 0.1 M KOH aqueous solution before and after 1000 cycles of CV curves with a scan rate of 50 mV/s (a). Current-time chronoamperometric responses of the commercial 20 wt% Pt/C and CS₁₂₋₆₅₀ at 0.75 V in O₂-saturated 0.1 M KOH aqueous solution followed by addition of 3.0 M methanol. The rotation rate is 1600 rpm (b).

3. Materials and Methods

3.1. Materials

Iron(III) chloride hexahydrate, 4-formylphenylboronic acid and 3,4-dihydroxybenzaldehyde were purchased from Aladdin Company (Shanghai, China) and directly used as received. Tris(4-aminophenyl)amine was obtained from J&K Chemical (Beijing, China). KOH, anhydrous methanol and anhydrous ethanol were supplied by Shanghai Chemical Reagent Industry (Shanghai, China). Nafion (5 wt%) was purchased from Sigma-Aldrich (St. Louis, MO, USA). Boronic monomer TBB was synthesized through our reported method [23]. The catechol monomer DFC was directly synthesized through the Schiff base formation reaction between 4,4'-(((perfluoropropane-2,2-diyl)bis(4,1-phenylene))bis(oxy)dianiline and 3,4-dihydroxybenzaldehyde (detailed procedure is described in Supporting Information).

3.2. Catalyst Preparation

DFC and TBB were dissolved in methanol to afford a concentration of 1.0 mg/mL. TBB solution (6 mL, 0.087 mmol) was added into DFC solution (10 mL, 0.132 mmol) dropwise under N₂ atmosphere with vigorous stirring. The mixture solution became deep orange and a suspension of boronate polymer nanospheres (BPN) formed. BPN powder was obtained by centrifugation and washed with anhydrous methanol three times.

BPN was redispersed in 16 mL of methanol to get 2.0 mg/mL of particle suspension. Then 2.37 mL of methanol solution of FeCl₃ (10 mg/mL, 0.037 mmol/mL) was added to the suspension of BPN. After different reaction times, such as 6, 12 and 18 h, the resultant hollow particles were collected by centrifugation, washed by anhydrous methanol, and then dried in vacuum oven at 50 °C overnight. The hollow particles were firstly carbonized at 650 °C for 2 h in an argon atmosphere with a fixed heating rate of 5 °C /min. The second carbonation was performed at 650 °C for 1 h in a mixture gas containing 5% hydrogen and 95% argon with a fixed heating rate of 10 °C /min to reduce Fe³⁺ into Fe, thus forming B, N, F and Fe co-doped hollow carbon nanospheres (denoted as CSs). CS₆₋₆₅₀, CS₁₂₋₆₅₀ and CS₁₈₋₆₅₀ represent carbon shells prepared from 6, 12 and 18 h reaction times between BPN and FeCl₃, respectively. To evaluate the carbonization temperature on the electrochemical properties of carbon shells, control experiments were performed at pyrolysis temperatures of 550 and 750 °C, and the prepared samples were denoted as CS₁₂₋₅₅₀ and CS₁₂₋₇₅₀.

3.3. Characterization

The scanning electron microscopy (SEM) were characterized using an SU-70 microscope (HITACHI, Tokyo, Japan). The morphology of the samples was tested by transmission electron microscopy (JEM-2100) (JEOL, Tokyo, Japan). The high-angle annular dark-field scanning transmission electron microscopy (HAADF-STEM) images, elemental energy-dispersive X-ray spectroscopy (EDX) mapping and line scanning analyses were acquired on a FEI TECNAI F20 microscope (Hillsboro, OR, USA) tested at 200 kV. The Raman spectra were tested on a Labram HR800 Evolution (Horiba, Lille, France). The powder X-ray diffraction (XRD) patterns were obtained through a desktop X-ray Diffractometer using Cu (600 W) K α radiation (Rigaku, Tokyo, Japan) to characterize the crystallographic structure of the samples. The Brunauer–Emmett–Teller (BET) surface area and pore volume of the samples were tested through an ASAP 2460 system (Norcross, GA, USA). Before measurement, all of the samples were uniformly degassed at 120 °C for 12 h under vacuum before the test. The X-ray photoelectron spectroscopy (XPS) was tested by PHI Quantum-2000 photoelectron spectrometer (Physical Electronics, Inc., Chanhassen, MN, USA) through a monochromatic Al X-ray source of K α radiation (1486.6 eV), and all of the spectra had been calibrated with the C 1s peak at 284.6 eV as an internal standard.

3.4. Electrochemical Measurements

The electrochemical properties of the samples were measured on an electrochemical workstation (CHI 760E), through a conventional three-electrode system. Before testing, 5.0 mg of CSs was dispersed in 1.0 mL of a mixed solvent containing anhydrous ethanol (500 μ L), H₂O (450 μ L) and 5 wt% Nafion (50 μ L). The above slurry (4.5 μ L) was dropped onto a glassy carbon electrode and used as working electrode. The quality of the commercial 20 wt% Pt/C was half of the CSs catalyst. ORR performance was tested in freshly made KOH aqueous solution (0.1 M) at room temperature. Pt foil and an Ag/AgCl (KCl saturation) electrode were used as the counter electrode and the reference electrode, respectively. The potential in this article was relative to the Ag/AgCl electrode.

4. Conclusions

In summary, a new type of carbon shell co-doped with multi-element including B, N, F and Fe was designed and synthesized. The morphology and the content of the Fe element of the carbon

shell could be easily tuned by changing the reaction time between the boronate polymer and Fe^{3+} . The CS_{12-650} catalyst showed excellent catalytic activity toward ORR ($E_{\text{onset}} = 0.91$ V, $E_{\text{half-wave}} = 0.82$ V vs. RHE), which were comparable to commercial Pt/C in an alkaline system. We verified that the existence of the fluorine element in the carbon matrix was important for the improvement of ORR performance. From the prospective of methodology, we consider that the Kirkendall effect-based route to metallosupramolecular polymer hollow spheres may be of great interest in the design of precursors incorporated with transition metal elements, thereby generating high-performance doped carbon materials.

Supplementary Materials: The following are available online at <http://www.mdpi.com/2073-4344/9/1/102/s1>, Synthetic routes of DFC and TBB, TEM image of CS_{12-550} and CS_{12-750} , the corresponding K-L plots of CSs, XPS survey spectra CS_{12-550} and CS_{12-750} , the atomic percent of elements of CS_{12-750} and LSV curves of the commercial 20 wt% Pt/C before and after 1000 cycles of CV curves are in the supporting information.

Author Contributions: The experiments were designed by C.Y. and L.D. The experiment was carried out and the manuscript was written by Y.W. The data were analyzed by Y.L., J.M., H.W., T.W., Y.L., B.Z. and Y.X.

Funding: This work was supported by the National Natural Science Foundation of China (51673161, 51773172), Scientific and Technological Innovation Platform of Fujian Province (2014H2006).

Conflicts of Interest: The authors declare no conflict of interest.

References

1. Shao, M.H.; Chang, Q.W.; Dodelet, J.P.; Chenitz, R. Recent Advances in Electrocatalysts for Oxygen Reduction Reaction. *Chem. Rev.* **2016**, *116*, 3594–3657. [[CrossRef](#)] [[PubMed](#)]
2. Kulkarni, A.; Siahrostami, S.; Patel, A.; Nørskov, J.K. Understanding Catalytic Activity Trends in the Oxygen Reduction Reaction. *Chem. Rev.* **2018**, *118*, 2302–2312. [[CrossRef](#)] [[PubMed](#)]
3. Mano, N.; Poulpiquet, A.D. O_2 Reduction in Enzymatic Biofuel Cells. *Chem. Rev.* **2018**, *118*, 2392–2468. [[CrossRef](#)] [[PubMed](#)]
4. Kakati, N.; Maiti, J.; Lee, S.; Jee, S.H.; Viswanathan, B.; Yoon, Y.S. Anode catalysts for direct methanol fuel cells in acidic media: Do we have any alternative for Pt or Pt-Ru? *Chem. Rev.* **2014**, *114*, 12397–12429. [[CrossRef](#)] [[PubMed](#)]
5. Pegis, M.L.; Wise, C.F.; Martin, D.J.; Mayer, J.M. Oxygen Reduction by Homogeneous Molecular Catalysts and Electrocatalysts. *Chem. Rev.* **2018**, *118*, 2340–2391. [[CrossRef](#)] [[PubMed](#)]
6. Fu, S.F.; Zhu, C.Z.; Song, J.H.; Engelhard, M.H.; Xia, H.B.; Du, D.; Lin, Y.H. Kinetically Controlled Synthesis of Pt-Based One-Dimensional Hierarchically Porous Nanostructures with Large Mesopores as Highly Efficient ORR Catalysts. *ACS Appl. Mater. Interfaces* **2016**, *8*, 35213–35218. [[CrossRef](#)]
7. Unwin, P.R.; Guell, A.G.; Zhang, G.H. Nanoscale Electrochemistry of sp (2) Carbon Materials: From Graphite and Graphene to Carbon Nanotubes. *Acc. Chem. Res.* **2016**, *49*, 2041–2048. [[CrossRef](#)]
8. Rao, C.V.; Viswanathan, B. ORR Activity and Direct Ethanol Fuel Cell Performance of Carbon-Supported Pt-M (M = Fe, Co, and Cr) Alloys Prepared by Polyol Reduction Method. *Phys. Chem. C* **2009**, *113*, 18907–18913.
9. Kim, J.H.; Sa, Y.J.; Jeong, H.Y.; Joo, S.H. Roles of Fe-N_x and Fe-Fe₃C@C Species in Fe-N/C Electrocatalysts for Oxygen Reduction Reaction. *ACS Appl. Mater. Interfaces* **2017**, *9*, 9567–9575. [[CrossRef](#)]
10. Zhang, Q.; Mamtani, K.; Jain, D.; Ozkan, U.; Asthagiri, A. CO Poisoning Effects on FeNC and CN_x ORR Catalysts: A Combined Experimental-Computational Study. *J. Phys. Chem. C* **2016**, *120*, 15173–15184. [[CrossRef](#)]
11. Loget, G.; Zigah, D.; Bouffier, L.; Sojic, N.; Kuhn, A. Bipolar electrochemistry: From materials science to motion and beyond. *Acc. Chem. Res.* **2013**, *4*, 2513–2523. [[CrossRef](#)] [[PubMed](#)]
12. Ambrosi, A.; Chua, C.K.; Bonanni, A.; Pumera, M. Electrochemistry of graphene and related materials. *Chem. Rev.* **2014**, *114*, 7150–7188. [[CrossRef](#)]
13. Ghasemi, M.; Daud, W.R.W.; Hassan, S.H.A.; Ismail, O.; Rahimnejad, M.; Jahim, J.M. Nano-structured carbon as electrode material in microbial fuel cells: A comprehensive review. *J. Alloy Compd.* **2013**, *580*, 245–255. [[CrossRef](#)]

14. Lin, F.; Liu, Y.J.; Yu, X.Q.; Cheng, L.; Singer, A.; Shpyrko, O.G.; Huolin, L.; Xin, L.H.; Tamura, N.; Tian, C.X.; et al. Synchrotron X-ray Analytical Techniques for Studying Materials Electrochemistry in Rechargeable Batteries. *Chem. Rev.* **2017**, *117*, 13123–13186. [[CrossRef](#)] [[PubMed](#)]
15. Tong, X.; Wei, Q.L.; Zhan, X.X.; Zhang, G.X.; Shu, H.; Sun, S.H. The New Graphene Family Materials: Synthesis and Applications in Oxygen Reduction Reaction. *Catalysts* **2017**, *7*, 1. [[CrossRef](#)]
16. Brouzgou, A.; Song, S.Q.; Liang, Z.X.; Tsiakaras, P. Non-Precious Electrocatalysts for Oxygen Reduction Reaction in Alkaline Media: Latest Achievements on Novel Carbon Materials. *Catalysts* **2016**, *6*, 159. [[CrossRef](#)]
17. Wu, Z.X.; Song, M.; Wang, J.; Liu, X. Recent Progress in Nitrogen-Doped Metal-Free Electrocatalysts for Oxygen Reduction Reaction. *Catalysts* **2018**, *8*, 196. [[CrossRef](#)]
18. Paraknowitsch, J.P.; Thomasa, A. Doping carbons beyond nitrogen: An overview of advanced heteroatom doped carbons with boron, sulphur and phosphorus for energy applications. *Energy Environ. Sci.* **2013**, *6*, 2839–2855. [[CrossRef](#)]
19. Bag, S.; Roy, K.; Gopinath, C.; Raj, C.R. Facile single-step synthesis of nitrogen-doped reduced graphene oxide-Mn(3)O(4) hybrid functional material for the electrocatalytic reduction of oxygen. *ACS Appl. Mater. Interfaces* **2014**, *6*, 2692–2699. [[CrossRef](#)] [[PubMed](#)]
20. Xiong, D.B.; Li, X.F.; Fan, L.L.; Bai, Z.M. Three-Dimensional Heteroatom-Doped Nanocarbon for Metal-Free Oxygen Reduction Electrocatalysis: A Review. *Catalysts* **2018**, *8*, 301. [[CrossRef](#)]
21. Liu, J.; Ji, Y.G.; Qiao, B.; Zhao, F.Q.; Gao, H.X.; Chen, P.; An, Z.W.; Chen, X.B.; Chen, Y. N, S Co-Doped Carbon Nanofibers Derived from Bacterial Cellulose/Poly (Methylene Blue) Hybrids: Efficient Electrocatalyst for Oxygen Reduction Reaction. *Catalysts* **2018**, *8*, 269. [[CrossRef](#)]
22. Kim, D.W.; Li, O.L.; Saito, N. Enhancement of ORR catalytic activity by multiple heteroatom-doped carbon materials. *Phys. Chem. Chem. Phys.* **2015**, *17*, 407–413. [[CrossRef](#)]
23. Chang, Y.; Yuan, C.H.; Li, Y.T.; Liu, C.; Wu, T.; Zeng, B.R.; Xu, Y.T.; Dai, L.Z. Controllable fabrication of a N and B co-doped carbon shell on the surface of TiO₂ as a support for boosting the electrochemical performances. *J. Mater. Chem. A* **2017**, *5*, 1672–1678. [[CrossRef](#)]
24. Chang, Y.; Yuan, C.H.; Liu, C.; Mao, J.; Li, Y.T.; Wu, H.Y.; Wu, Y.Z.; Xu, Y.T.; Dai, L.Z. B, N co-doped carbon from cross-linking induced self-organization of boronate polymer for supercapacitor and oxygen reduction reaction. *J. Power Sources* **2017**, *365*, 354–361. [[CrossRef](#)]
25. Bezerra, C.W.B.; Zhang, L.; Lee, K.C.; Liu, H.S.; Marques, A.L.B.; Marques, E.P.; Wang, H.J.; Zhang, J.J. A review of Fe-N/C and Co-N/C catalysts for the oxygen reduction reaction. *Electrochim. Acta* **2008**, *53*, 4937–4951. [[CrossRef](#)]
26. Liua, Y.Y.; Yue, X.P.; Li, K.X.; Qiao, J.L.; Wilkinsone, D.; Zhang, J.J. PEM fuel cell electrocatalysts based on transition metal macrocyclic compounds. *Coord. Chem. Rev.* **2016**, *315*, 153–177. [[CrossRef](#)]
27. Guo, J.N.; Cheng, Y.H.; Xiang, Z.H. Confined-Space-Assisted Preparation of Fe₃O₄ Nanoparticle Modified Fe-N-C Catalysts Derived from a Covalent Organic Polymer for Oxygen Reduction. *ACS Sustain. Chem. Eng.* **2017**, *5*, 7871–7877. [[CrossRef](#)]
28. Liu, J.; Li, E.L.; Ruan, M.B.; Song, P.; Xu, W.L. Recent Progress on Fe/N/C Electrocatalysts for the Oxygen Reduction Reaction in Fuel Cells. *Catalysts* **2015**, *5*, 1167–1192. [[CrossRef](#)]
29. Jiang, W.J.; Gu, L.; Li, L.; Zhang, Y.; Zhang, X.; Zhang, L.J.; Wang, J.Q.; Hu, J.S.; Wei, Z.D.; Wan, L.J. Understanding the High Activity of Fe-N-C Electrocatalysts in Oxygen Reduction: Fe/Fe₃C Nanoparticles Boost the Activity of Fe-N(x). *J. Am. Chem. Soc.* **2016**, *138*, 3570–3578. [[CrossRef](#)]
30. Li, L.Y.; Yuan, C.H.; Dai, L.Z. Thermoresponsive Polymeric Nanoparticles: Nucleation from Cooperative Polymerization Driven by Dative Bonds. *Macromolecules* **2014**, *47*, 5869–5876. [[CrossRef](#)]
31. Li, L.Y.; Yuan, C.Y.; Zhou, D.M.; Ribbe, D.E.; Kittilstved, P.R.; Thayumanavan, S. Utilizing Reversible Interactions in Polymeric Nanoparticles to Generate Hollow Metal-Organic Nanoparticles. *Angew. Chem. Int. Ed.* **2015**, *127*, 13183–13187. [[CrossRef](#)]
32. Ejima, H.; Richardson, J.J.; Liang, K.; Best, J.P.; Koeverden, M.P.; Such, G.H.; Cui, J.W.; Such, G.H.; Cui, J.W.; Caruso, F. One-step assembly of coordination complexes for versatile film and particle engineering. *Science* **2013**, *341*, 154–157. [[CrossRef](#)]
33. Rahim, M.A.; Bjornmalm, M.; Suma, T.; Faria, M.; Ju, Y.; Kempe, K.; Mglner, M.; Ejima, H.; Stickland, A.D.; Caruso, F. Metal-Phenolic Supramolecular Gelation. *Angew. Chem. Int. Ed.* **2016**, *55*, 13803–13807. [[CrossRef](#)]

34. Barrett, D.G.; Fullenkamp, D.E.; He, L.H.; Holten, N.; Lee, K.C. pH-Based Regulation of Hydrogel Mechanical Properties Through Mussel-Inspired Chemistry and Processing. *Adv. Funct. Mater.* **2013**, *23*, 1111–1119. [[CrossRef](#)]
35. He, J.R.; Luo, L.; Chen, Y.F.; Manthiram, A. Yolk-Shelled C@Fe₃O₄ Nanoboxes as Efficient Sulfur Hosts for High-Performance Lithium-Sulfur Batteries. *Adv. Mater.* **2017**, *29*, 1702707. [[CrossRef](#)] [[PubMed](#)]
36. Liu, X.X.; Wang, Y.H.; Dong, L.; Chen, X.; Xin, G.X.; Zhang, Y.; Zang, J.B. One-step synthesis of shell/core structural boron and nitrogen co-doped graphitic carbon/nanodiamond as efficient electrocatalyst for the oxygen reduction reaction in alkaline media. *Electrochim. Acta* **2016**, *194*, 161–167. [[CrossRef](#)]
37. Sun, X.J.; Zhang, Y.W.; Song, P.S.; Pan, J.; Zhuang, L.; Xu, W.L.; Xing, W. Fluorine-Doped Carbon Blacks: Highly Efficient Metal-Free Electrocatalysts for Oxygen Reduction Reaction. *ACS Catal.* **2013**, *3*, 1726–1729. [[CrossRef](#)]
38. Ali-Löytty, H.; Louie, M.W.; Singh, M.R.; Li, L.; Casalongue, H.G.; Ogasawara, H.; Crumlin, E.J.; Liu, Z.; Bell, A.T.; Nilsson, A.; et al. Ambient-Pressure XPS Study of a Ni-Fe Electrocatalyst for the Oxygen Evolution Reaction. *J. Phys. Chem. C* **2016**, *120*, 2247–2253. [[CrossRef](#)]
39. Wang, H.Y.; Iyyamperumal, E.; Roy, A.; Xue, Y.H.; Yu, D.S.; Dai, L.M. Vertically aligned BCN nanotubes as efficient metal-free electrocatalysts for the oxygen reduction reaction: A synergetic effect by co-doping with boron and nitrogen. *Angew. Chem. Int. Ed.* **2011**, *50*, 11756–11760. [[CrossRef](#)]



© 2019 by the authors. Licensee MDPI, Basel, Switzerland. This article is an open access article distributed under the terms and conditions of the Creative Commons Attribution (CC BY) license (<http://creativecommons.org/licenses/by/4.0/>).